Sensors & Actuators: A. Physical 378 (2024) 115780

Contents lists available at ScienceDirect

Sensors and Actuators: A. Physical

journal homepage: www.journals.elsevier.com/sensors-and-actuators-a-physical

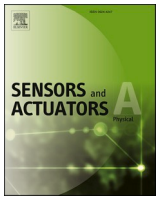

Dual-mode Shear Horizontal / Rayleigh-like surface-acoustic-wave configuration on lithium niobate 64° Y-cut

F. Lunardelli [b,c], M. Agostini [b], E. Corradi [c], M. Cecchini [a,*]

[a] NEST, Istituto Nanoscienze-CNR, Piazza San Silvestro 12, Pisa 56126, Italy
[b] INTA S.r.l., Intelligent Acoustics Systems, Via Nino Pisano 14, Pisa 56122, Italy
[c] NEST, Scuola Normale Superiore, Piazza San Silvestro 12, Pisa 56126, Italy

ARTICLE INFO

Keywords:
Surface acoustic waves
SAW
Dual-mode SAW excitation
SAW sensor
Acoustic
Streaming
Lithium niobate
Acoustic sensor

ABSTRACT

Technologies based on surface acoustic waves (SAWs) find widespread use in wireless communications, signal processing, and sensing applications. In this study, we present an innovative dual-mode SAW configuration using a 64° Y-cut lithium niobate (LN) substrate. The conventional setup, employing interdigital transducers (IDTs) oriented along the crystal X-axis, is known for generating the shear horizontal mode (SH-SAW) with in-plane polarization. Conversely, by utilizing IDTs oriented perpendicular to the X-axis, we introduce effective excitation of a Rayleigh-like SAW (R-SAW), a novel achievement in our research. Through finite element simulations and electro-mechanical analyses, we comprehensively characterize these modes in terms of frequencies, polarizations, propagation losses, and temperature coefficients. Furthermore, we investigate their interaction with liquids by analyzing damping characteristics and acoustic streaming effects using particle image velocimetry (PIV). SH-SAWs exhibit a leaky displacement during propagation with minimal damping in liquids, resulting in weak acoustic streaming—ideal for real-time sensing applications in wet environments. In contrast, non-leaky R-SAWs, characterized by a strong displacement component normal to the surface, exhibit enhanced acoustic streaming, facilitating microfluidic operations. Additionally, R-SAWs demonstrate high sensitivity to mass loading, making them optimal for real-time sensing in dry environments. The ability to generate both SAW modes on the same substrate offers the potential to develop fully electrical-driven, multifunctional integrated sensing platforms with SAW-driven microfluidic capabilities. This unique capability promises novel solutions in bio-sensing, leveraging the complementary strengths of the two acoustic modes in detection and sample handling.

1. Introduction

Surface acoustic waves (SAWs) are acoustic waves confined to the surface of a substrate, with a penetration depth of a few wavelengths. SAW devices can excite and detect waves by exploiting a piezoelectric crystal substrate and metallic interdigital transducers (IDTs) patterned on it. Technologies based on SAWs are widely used for many applications, such as wireless communications, signal processing, and sensing [1]. Among these, the development of high-performance sensors is possible thanks to the fact that SAWs are very sensitive to surface perturbations, such as mass adhesion, temperature, pressure, and viscosity changes [2]. These characteristics, combined with the possibility of integrating SAW-driven microfluidics, make SAW devices one of the most promising technologies for the realization of electrically driven lab-on-chips (LoCs) [3]. SAW-based LoCs stand out for their capability to integrate various operations—like analyte detection, particle and fluid manipulation in a single, electrically controlled device, characterized by miniaturization, low power consumption, and adaptability.

A key challenge in this field is enhancing SAW sensor performance, such as multiplexed analysis and fluidic manipulation, by exciting different SAW types on the same substrate. Two primary SAW types are shear horizontal (SH-SAWs) and Rayleigh (R-SAWs), differentiated by their polarization. SH-SAWs, with their in-plane horizontal polarization, are suitable for liquid environment applications and enable real-time detection in continuous flow [4]. R-SAWs have an elliptical polarization in the sagittal plane with a strong component normal to the surface. They are highly sensitive in detecting surface perturbations, but cannot be used for real-time detection in liquids, due to damping. However,

* Corresponding author.
E-mail address: marco-cecchini@cnr.it (M. Cecchini).

https://doi.org/10.1016/j.sna.2024.115780
Received 3 May 2024; Received in revised form 12 July 2024; Accepted 4 August 2024
Available online 21 August 2024

their interaction with liquids facilitates various fluid manipulation operations essential in LoC devices like pumping, droplet actuation, particle separation or concentration and mixing [5–8].

The choice of the piezoelectric substrate, together with the definition of the SAW propagation direction (IDTs orientation), define the type of acoustic wave. If the sagittal plane, determined by the direction of wave propagation and its normal counterpart, is a plane of mirror symmetry for the crystal, then the primary wave mode is the Rayleigh mode. Otherwise, SH-SAWs are typically obtained [9].

To the best of our knowledge, only a few bulk piezoelectric substrates have been reported in the literature to support the generation of both SH-SAWs and R-SAWs in the same acoustic device and utilize them for sensing applications. The first substrate is the 37° Y-cut quartz, where R-SAWs are excited along the x-direction and SH-SAWs along the perpendicular direction [10]. The paper presents a one-chip biosensor system that uses SH-SAW for sensing and R-SAW for agitation. Its performance was tested by detecting the adhesion of the C-reactive protein antibody, demonstrating that the reaction can be accelerated by R-SAW mixing. Another work on 37° Y-cut quartz by Shuangming Li et al. [11] highlighted the removal of nonspecifically bound proteins achieved through R-SAW agitation. Wenyi Huang et al. demonstrate the implementation of SH-SAW biosensing with the exploitation of a Rayleigh wave-streaming function on the same miniaturized bio-chip of 42.5° Y-cut quartz (ST-cut). [12] On the 148° X-cut lithium tantalate substrate, SH-SAW and R-SAW with different frequencies can be effectively generated using a tilted IDTs [13]. In this case as well, the dual functionality of the acoustic waves (sensing and mixing) resulted in improved biosensing. Additionally, there is research exploring the properties of langasite piezoelectric substrate for biosensing and biofouling removal [14]. Similar to the 37° Y-cut quartz, a system with an orthogonal IDTs is used.

Our work focuses on the SAW properties of the 64° Y-cut lithium niobate (LN) substrate. This substrate, as Yamanouchi et al. demonstrated [15], efficiently generates SH-SAWs along the X-axis with a strong electromechanical coupling coefficient k^2= 11.3 % and a quite high propagation velocity (4474 m/s for the metalized surface). The same authors also specified that “Rayleigh waves at 64° Y-cut LN almost could not be observed owing to their small coupling coefficients”. These characteristics of the 64° Y-cut LN are particularly suitable for liquid sensing applications. A significant example is represented by the SH-SAW sensor for the detection of heavy metal compounds, described in the work of Ramshani et al. [16].

We have here developed and tested a SAW device based on a 64° Y-cut LN to explore and characterize the different acoustic modes that can be excited in this specific substrate. Our focus was particularly on examining the potential for generating wave types other than SH-SAW with IDTs orientations differing from the X-axis. To achieve this, we initially conducted simulations using Finite Element Method (FEM), where we explored various IDTs orientations. Then we fabricated a real device with gold electrodes patterned on 64° Y-cut LN oriented in two main directions: parallel and orthogonal to the X-axis. We conducted an electrical characterization of the different acoustic modes by measuring the resonance spectra through a Vector Network Analyzer (VNA) in both dry and liquid environments. We carried out a mechanical characterization by using a laser Doppler vibrometer to reconstruct and compare the normal displacement of the different acoustic modes. This type of measurement provided us with important information regarding the polarization of the different acoustic modes. Afterward, we conducted acoustic streaming experiments to assess how these different modes interact with the liquid. We processed the signals using particle image velocimetry (PIV). Finally, we tested the responses of the different waves to external changes, such as temperature variation, with the aim of obtaining a temperature coefficient of frequency (TCF).

2. Materials and methods

2.1. Finite element method

The surface acoustic waves propagating along the surface of a piezoelectric substrate are well described by the following constitutive equations:

$$\begin{cases} c_{ijkl}\dfrac{\partial^2 u_k}{\partial x_j \partial x_l} + e_{ijk}\dfrac{\partial^2 \Phi}{\partial x_j \partial x_k} - \rho\dfrac{\partial^2 u_i}{\partial^2 t} = 0 \\ e_{jkl}\dfrac{\partial^2 u_k}{\partial x_j \partial x_l} - \varepsilon_{jk}\dfrac{\partial^2 \Phi}{\partial x_j \partial x_k} = 0 \end{cases} \quad (1)$$

where $i,j,k,l = 1, 2, 3$, c_{ijkl}, e_{ijk}, ε_{jk} are the elastic, piezoelectric and dielectric constants respectively, u_i mechanical displacement, ρ the density, Φ the electrical potential.

In the Finite Element Method (FEM), the geometry of the entire system is divided into smaller, interconnected units called finite elements. These elements are linked at nodes, which are points shared by two or more units, as well as along boundary lines. This numerical method applies constitutive equations to each finite element individually and then combines these to generate a solution for the whole system [17]. To further simplify the simulation geometry without losing information, the approximation of a periodic unit cell was used. In SAW devices, IDTs may have from ten to hundreds of identical electrodes, and each electrode can be about 100 times longer than their width. Therefore, it is possible to neglect the edge effects and reduce the model geometry to the periodic unit cell [18].

The simulations were conducted using the COMSOL Multiphysics software, incorporating the piezoelectric effect module that integrates solid mechanics and electrostatics.

Fig. 1 illustrates the unit cells of the models simulated, focusing on specific orientations of IDTs, each featuring a pair of gold electrode

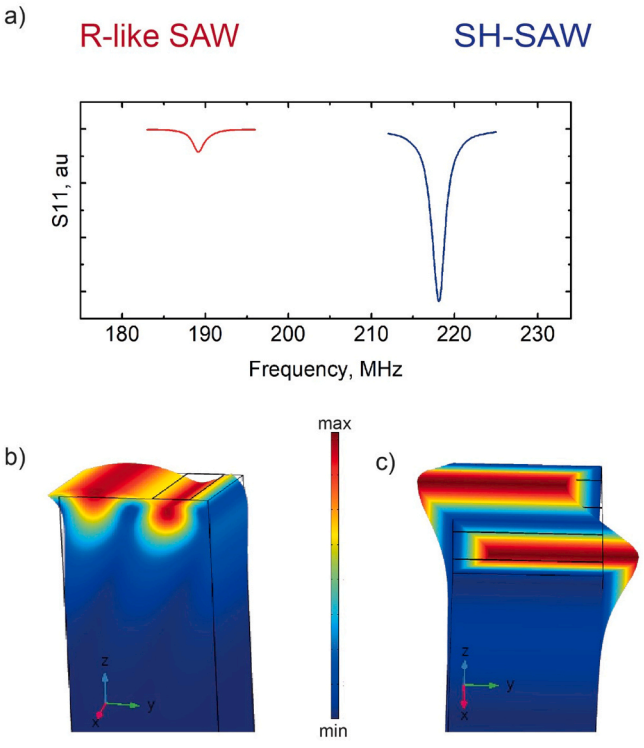

Fig. 1. Finite element simulation results of unit cell models, focused on frequency study and polarization analysis. **a)** S11 simulated spectra of R-like SAW and SH-SAW. **b)** 3D unit cell model representing the displacement of R-like SAW. **c)** 3D unit cell model representing the displacement of SH-SAW.

patterns on a piezoelectric substrate of 64° Y-cut LN. The unit cell's size corresponds to the selected wavelength, λ=20 μm, leading to an electrode width of λ/4=5 μm with a thickness of 100 nm. For these unit cell models, periodic boundary conditions have been established on the lateral surfaces, encompassing both solid mechanics and electrostatics aspects. Parameters such as the elasticity matrix, the coupling matrix, and the relative permittivity were set to define the properties of the 64° Y-cut LN 64° Y-cut substrate.

For conducting a frequency domain analysis, one electrode is designated as a terminal with an input power of 1 W, while the other electrode is grounded. This periodic modelling approach enables the determination of resonant frequencies, mode shapes, and the distribution of displacement of the SAW generated on this substrate.

2.2. Device design and fabrication

We utilized a 64° Y-cut LN substrate (Nano Quartz Wafer, Langenzenn, Germany), on which patterns of two IDTs were fabricated (Fig. 2). Each IDT consists of 30 finger pairs with a 50 % metallization ratio and electrodes width of 5 μm. The acoustic aperture for each IDTs is 250 μm. The electrodes are made of gold (Au) and have a thickness of 100 nm. In addition, there is an adhesive layer between the gold and the substrate, consisting of 10 nm of titanium (Ti). To explore different acoustic modes, as depicted in Fig. 2, one IDT is oriented along the X crystallographic axis and the other in the perpendicular direction, corresponding respectively to the x-direction and y-direction of our coordinate system.

The fabrication process began with the deposition of a bilayer of titanium (Ti, 10 nm) and gold (Au, 100 nm) using a thermal evaporator from Kurt J. Lesker. The design of IDTs was then defined through optical lithography on a layer of negative photoresist, specifically ma-N 1407 from Microresist Technology, using a laser writer (MicroWriter ML3, Durham Magneto Optics). The final etching stage involved reactive ion etching (RIE) using a system from Sistec. This process used argon at 0.9 mbar and 50 W for 15 minutes to remove the unexposed Au, followed by wet etching with a piranha solution (H2SO4:H2O2 in a 3:1 vol ratio) for 2 minutes to remove the Ti layer. Each chip presented four pairs of IDTs, which were connected to the RF system using coplanar waveguides and wire-bonded to a printed circuit board (PCB).

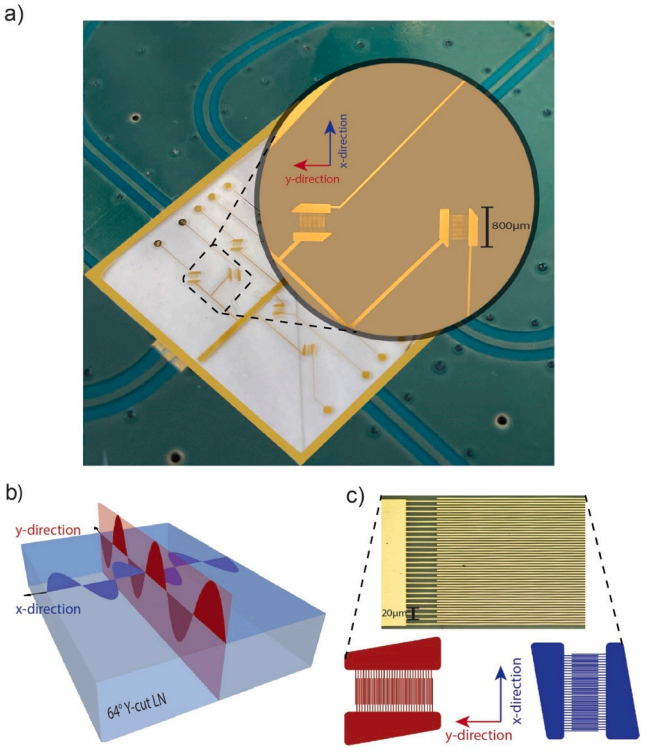

Fig. 2. a), c) Optical microscope images coupled with a CAD schematic depict the fabricated device, highlighting the geometry and orientation of the two Interdigital Transducers (IDTs). **b)** Schematic illustration of wave polarizations: a shear horizontal SAW (blue) propagating along the x-direction and a Rayleigh-like SAW (red) propagating along the direction perpendicular (y-direction).

2.3. Electromechanical characterization, measurements set-up

For the electrical measurements, we used a vector network analyzer (VNA, ENA Series Network Analyzer, E5071C, Agilent Technologies). Each measurement was taken with a frequency span of 40 MHz, 15000 data points, and a smoothing factor of 1.5 %. The mechanical measurements were performed using a laser Doppler vibrometer (LDV, UHF-120 Ultra High Frequency Vibrometer, Polytec). The reconstructions of normal displacement were achieved by selecting a scan area with a length of 12λ and applying a signal (tuned to resonance frequencies) with a power of 14 dBm. The trends of the wave amplitude as a function of the applied power were obtained by varying the power from 0 dBm to 20 dBm and measuring the maximum displacement. For determining the temperature coefficient of frequency (TCF), we used a temperature controller (TED-350, ThorLabs) connected to a Peltier cell in direct contact, through thermal paste, with the chip. The latter is mounted on a special perforated PCB to ensure the transmission of heat from the Peltier cell.

2.4. Acoustic streaming and PIV measurements

Acoustic streaming experiments were performed using a droplet containing a solution of latex beads (polystyrene, Sigma-Aldrich 1um mean particle size) in water. A 0.5 μL droplet was carefully placed in front of the IDTs, using a micropipette. RF signals (MXG Analog Signal Generator N5181A, Agilent Technologies), tuned to the resonance frequencies of the waves, were applied to the IDTs to generate acoustic streaming. The power of the RF signal varied in the range 0 dBm to 15 dBm. The movement of the latex beads (which is correlated to the fluid motion) was measured by transmitted light microscopy (*inverted Nikon Eclipse TI*). A high-speed monochrome camera was used to record particle movement at 555 fps. We reconstructed the induced streamlines and determined the streaming velocity by performing particle image velocimetry (PIV) analysis on the recorded videos.

3. Results

To investigate the characteristics of 64° Y-cut LN as a substrate supporting multiple modes of Surface Acoustic Waves (SAWs), we initially conducted finite element simulations using COMSOL Multiphysics software, as shown in Fig. 1. When the Interdigitated Transducers (IDTs) were aligned along the crystallographic X-axis, which coincides with the x-direction in the coordinate system, a notable dip in the reflection coefficient S11 occurred at 218.1 MHz (see Fig. 1a). Analysis of the displacement reconstruction (Fig. 1c, Table 1) revealed that this dip corresponds to a SAW predominantly characterized by

Table 1
Summary of the FEM analysis of the polarization at the resonance frequencies. Contribution of the different components to the total displacement $x_i = \frac{x_i}{\sqrt{x_i^2 + x_j^2 + x_k^2}}$. The orientations are referred to the system shown in Fig. 1.

Substrate	Wave	X displacement	Y displacement	Z displacement
64° Y-cut LN	SH-SAW	13 %	62 %	25 %
64° Y-cut LN	R-SAW	1 %	45 %	54 %
128° Y-cut LN	R-SAW	5 %	36 %	59 %

shear horizontal polarization, traveling at a velocity of 4362 m/s. In contrast, configuring the IDTs perpendicular to this direction, along the y-direction of the coordinate system, resulted in a dip in S11 at 189.2 MHz (Fig. 1a). The displacement of this acoustic mode lies in the sagittal plane with a strong component normal to the surface (Fig. 1b, Table 1). This behavior is consistent with the excitation of a Rayleigh-like SAW with propagation velocity of 3784 m/s. Fig. 1e illustrates the difference in acoustic coupling between the two acoustic modes, with the shear-horizontal mode being significantly deeper than the Rayleigh-like mode.

Through numerical simulations, the mechanical coupling coefficients of the two acoustic modes have been calculated (see supplementary materials for details), yielding to $k^2 = 9.42 \pm 0.05$ % for SH-SAW and $k^2 = 2.15 \pm 0.06$ % for Rayleigh-like SAW.

Following the FEM results, we realized a device consisting of sets of two IDTs having the same geometry described in previous section, one oriented along the X crystallographic axis and the other in the perpendicular direction, corresponding respectively to the x-direction and y-direction of our coordinate system (Fig. 2). In order to confirm the actual presence of the two acoustic modes, we performed both electrical and mechanical characterizations of the device. Fig. 3 displays the results of the S11 reflection spectrum measurements, carried out using a Vector Network Analyzer (VNA), for each IDT orientation. The IDT oriented along the X-axis produces a resonance in the S11 signal at 217.8 MHz (Fig. 3b), representing a SAW travelling at 4356 m/s. The system with the perpendicularly oriented IDT presents a resonance frequency at 190.3 MHz, indicative of a SAW travelling at 3806 m/s. To evaluate the coupling of the different acoustic modes, we calculated the Q-factors of the relative resonances (the ratio between the central frequency and the FWHM of the S11 spectrum peaks). For the SAW excited along the X-axis, we obtained a Q-factor of 54, while for the SAW in the perpendicular direction, a Q-factor of 33.

The mechanical characterization of the waves was carried out by the Laser Doppler Vibrometer (LDV), and it is summarized in Fig. 4. Pannel 4a shows the measurement of the displacement normal to the surface for the acoustic mode generated with IDTs along X-axis with a central frequency around 217 MHz. This scan highlights the SAW damping during propagation which is consistent with coupling with bulk acoustic waves. This result is in accordance with what we obtained from the penetration depth numerical analysis reported in Section 3 of the supplementary materials. The damping identifies this mode as a leaky-SAW. Differently, for the IDT in perpendicular direction, the mode with the resonance frequency around190 MHz presents an higher surface confinement, with no-leaky propagation (panel 4b).

The analysis of the normal amplitude as a function of power applied to the IDTs is reported in panel 4c. In both cases, the relationship between Displacement and Power followed an exponential trend well described by a fitting curve of the form $y = ab^x$. For the SAW generated along X-axis we have $a = 7$+-1 pm and $b = 1.14$+-0.01 while, for perpendicular IDTs $a = 32$+-8 pm and $b = 1.18$+-0.01.

The mechanical analysis underscores the differences in polarization between the two acoustic modes. To further elucidate these differences and to comprehensively characterize the SAWs, we investigated their interaction with liquids. We began by examining the changes in the resonance spectra when the IDTs were covered with a 2 µl droplet of DI water, as illustrated in Fig. 3a. For the IDTs oriented along the X-axis, the S11 signal in liquid (Fig. 3b, blue line) showed a 30 % attenuation and a frequency shift of 900 kHz compared to its dry counterpart. Fig. 3c reveals that, in the presence of liquid, the S11 signal for the perpendicularly oriented IDTs experienced an 80 % attenuation and an 800 kHz frequency shift compared to the dry condition. In this case the spectrum is significantly modified.

Then, we conducted acoustic-streaming experiments based on particle image velocimetry (PIV). As we have demonstrated, the acoustic waves induce a surface displacement normal to or within the surface in

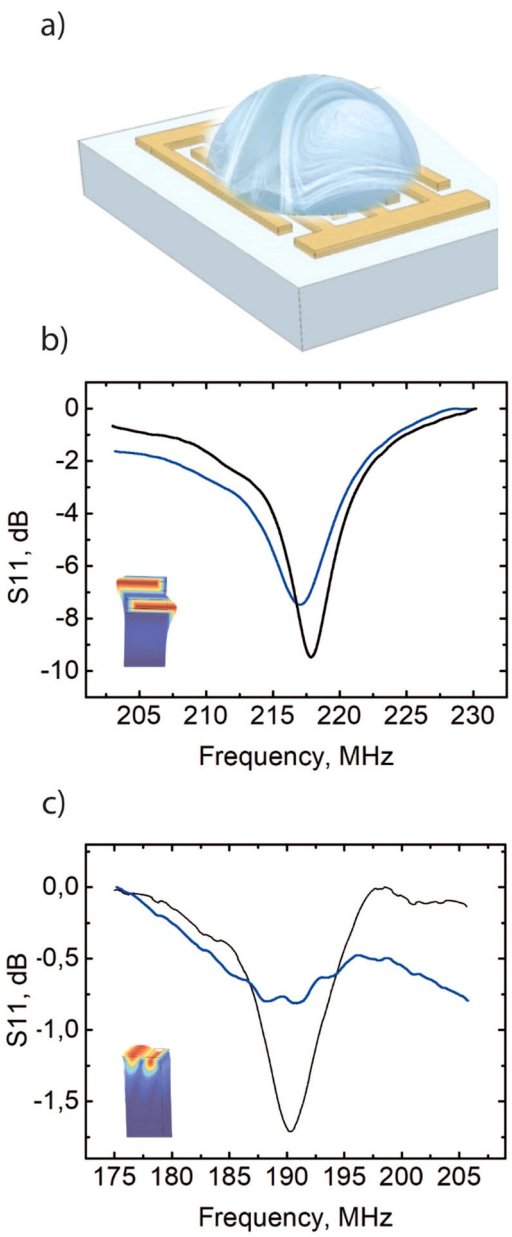

Fig. 3. VNA characterization of the waves in air and liquid environment. **a)** schematic representation of measurement set-up in liquid. **b)** S11 of shear horizontal SAW in air (black) and in water (blue). **c)** S11 of Rayleigh-like SAW in air (black) and in water (blue).

the range of a few angstroms to a few nanometers, depending on the applied powers and on the acoustic mode. When acoustic energy and momentum are coupled into the fluid, a net pressure forms in the direction of propagation of the acoustic wave and efficiently drives the liquid. This acoustically induced pressure generates the steady acoustic streaming that can be used for mixing and pumping [19]. Our objective was to evaluate the efficacy of these two wave types in fluid manipulation applications.

Fig. 5a illustrates the measurement setup: a 0.5 µl droplet containing water-dispersed latex beads was placed approximately 1 mm away from the IDTs. An RF generator, tuned to the resonance frequency of each wave type, generated the traveling SAWs that interacted with the droplet, inducing acoustic-streaming. To capture the particle movement, we used a transmitted light microscope equipped with a high-speed monochrome camera, recording at 555 frames per second (fps). The recorded footage (available in the supplementary materials) was

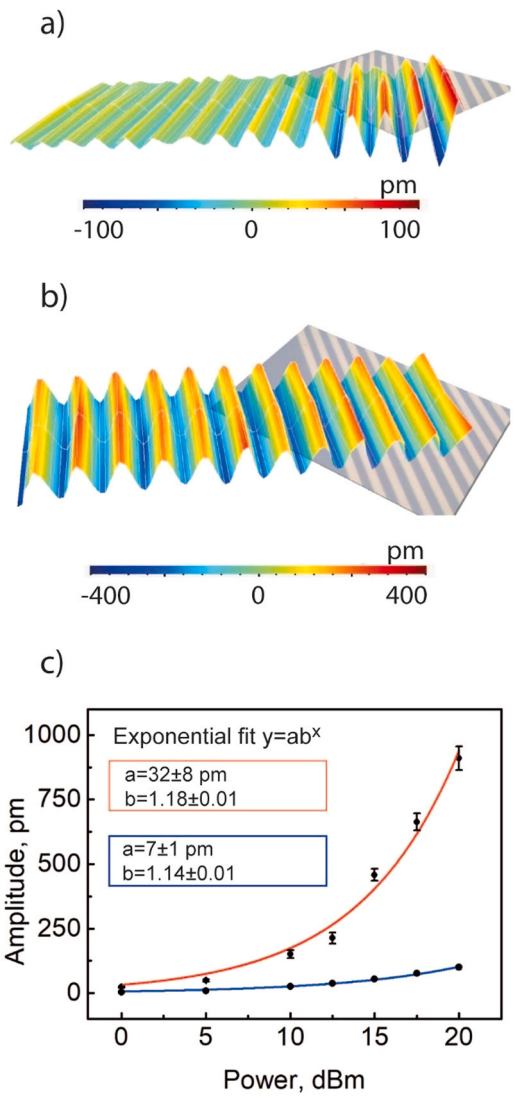

Fig. 4. LDV characterization of the waves. a) Reconstruction of the displacement normal to the surface of shear horizontal SAW. b) Reconstruction of the displacement normal to the surface of Rayleigh-like SAW. c) exponential trend of the amplitudes as a function of the applied power of both waves.

analyzed using PIV to map out the streamlines and associated velocity fields.

Figs. 5b and 5c present the streamline patterns and velocity fields, expressed in pixels per frame, for a stream induced by the wave parallel to the X-axis, excited with a 0 dBm power signal. The average streaming velocity, obtained through an appropriate scaling factor, in this instance was 42 ± 2 μm/s. However, the mode excited by perpendicularly aligned IDTs exhibited more efficient acoustic-streaming power transfer. At the same power level of 0 dBm, the average velocity achieved was significantly higher, reaching 370 ± 20 μm/s.

Finally, we tested the response of the two acoustic modes to external variations. By employing a Peltier cell coupled with a temperature controller, we were able to modify the temperature of the substrates. This allowed us to measure the resulting frequency shifts, which occur due to changes in the acoustoelastic properties and the temperature expansion coefficient of the material. The data, illustrated in Figs. 6a and 6b, exhibit a linear relationship between the frequency shift and the temperature changes. This observation aligns with previously documented findings related to SAW behavior on various other substrates, as referenced in the literature [20].

4. Discussion

FEM simulations highlighted the feasibility of exciting two distinct acoustic modes on 64° Y-cut LN using two perpendicularly oriented IDTs. The conventional setup with IDT along X-axis generates the well-known SH-SAW (Fig. 1c, Table1) with velocity in the range of 4300–4400 m/s and an electromechanical coupling coefficient $k^2 =$ 9.42 ± 0.05 % consistent with the literature (Morgan et al., 2007). On the other hand, an IDT configuration perpendicular to the X-axis yielded to a wave mode characterized by a strong component normal to the surface similarly to R-SAWs (Fig. 1b). As shown in Table 1, an identical simulation, conducted by changing 128° Y-cut LN as substrate and IDTs oriented along the X-axis (optimal configuration for R-SAW excitation) returned values of polarization similar with those obtained with the perpendicular acoustic mode (i.e the mode propagating along the y-direction) in 64° Y-cut LN. These simulation results have allowed us to define this acoustic mode as a Rayleigh-like SAW, with propagation velocity of 3700 m/s approximately and $k^2 = 2.15 \pm 0.06$ %.

Furthermore, through FEM, the penetration depths of the two acoustic modes were evaluated as reported in graph 2, Section 3 of the supplementary materials. For the Rayleigh-like SAW, there is a complete confinement of the acoustic mode energy within one wavelength from the surface, as an additional analogy with Rayleigh-SAW. For the SH-SAW mode, although the maximum energy values are maintained within a few wavelengths from the surface, there is the characteristic coupling with bulk waves. The electrical characterization of the device puts in evidence a good agreement between real data and simulation data. We obtained a similar S11 shape for each SAW and resonance frequencies with a difference from 0.1 % to 0.5 %. Based on this comparison, we can confirm the effective generation of SH-SAW parallel to the X-axis (as known in literature), and Rayleigh-like SAW along the perpendicular to X-axis. To the best of our knowledge, this latter acoustic mode, in this direction, represents a novelty for 64° Y-cut LN. Analyzing the coupling factors of these two modes via Q-factor calculation revealed that while SH-SAW is the dominant mode for this substrate, the Rayleigh-like (R-like) SAW is also significant and easily detectable.

The mechanical analysis via LDV scanning confirms the characteristics of the dual modes. SH-SAWs present a smaller out-of-plane displacement component, enabling us to visualize the mode and to assess its propagation beyond the IDT. As expected, this acoustic wave exhibits damping as it propagates, characterizing it as a leaky-SAW, in accordance with existing literature [21]. In contrast, R-like SAWs displayed a higher normal displacement compared to SH-SAWs and demonstrated non-leaky propagation. The amplitude of R-like SAWs is similar to those typically observed in 128°Y-X lithium niobate substrates, which are traditionally used for R-SAW excitation. The study "Ultra-high-frequency (UHF) surface-acoustic-wave (SAW) microfluidics and biosensors" by M. Agostini and M. Cecchini [22] details typical amplitudes for R-SAWs, usually ranging from tens of picometers to a few nanometers (comparable to those of R-like SAWs) and explores their applications in integrated sensing and mixing systems.

The interaction of these two modes with a liquid droplet placed on the IDTs highlights their polarization characteristics. For SH-SAW, the S11 spectrum shape (Fig. 3b) remains detectable in a liquid environment, exhibiting a Q-factor of 43. This suggests a relatively weak coupling of this wave in liquids. In contrast, the Rayleigh-like SAW experiences more significant damping in liquid due to its strong normal displacement component; Fig. 3c shows an 80 % attenuation of the S11 signal. The Q-factor for this mode is reduced to 21, and these spectra are characterized by notable noise levels, limiting the effectiveness of this wave for real-time detection in liquids.

Acoustic-streaming experiments, utilizing Particle Image Velocimetry (PIV), quantify the coupling of these acoustic modes with the liquid. Despite its weaker fluid coupling, the presence of SH-SAW induced

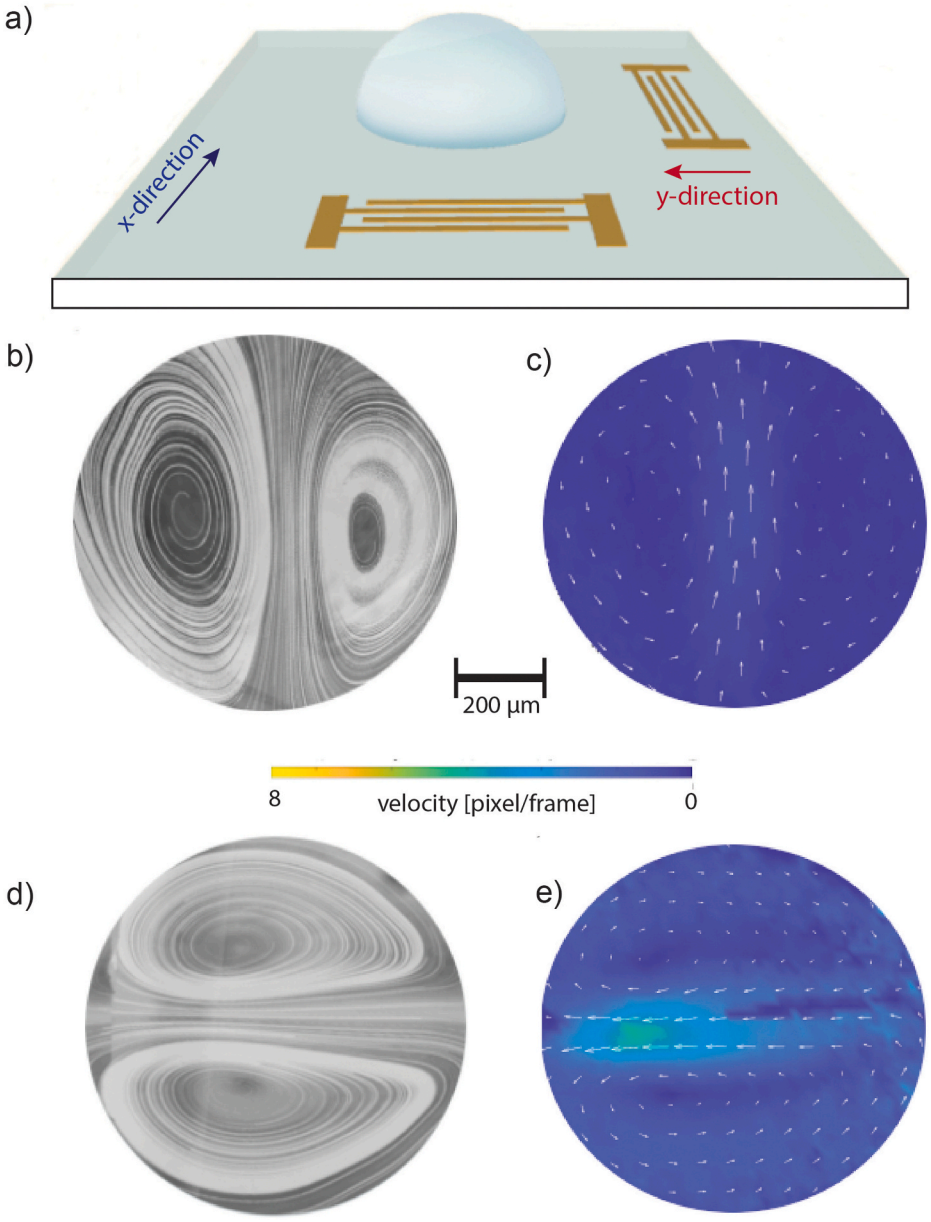

Fig. 5. Analysis of the acoustic streaming induced by the waves. (a) Schematic illustration of measurement set-up. A 0.5 µl water droplet containing beads for tracking the streaming has been positioned in front of the IDTs. (b), (c) PIV reconstruction of streamlines and of the velocity field induced by SH-SAW with a power of 0 dBm. (d), (e) PIV reconstruction of streamlines and of the velocity field induced by Rayleigh-like SAW with a power of 0 dBm.

acoustic-streaming was clearly observable. These results align with the findings in Brodie et al.'s study "Shear horizontal surface acoustic wave-induced microfluidic flow" [23], where the average velocity was 42 ± 2 µm/s. The mode excited by perpendicular IDTs, however, demonstrated more efficient power transfer in acoustic-streaming. Specifically, at 0 dBm power, the average velocity reached 370 ± 20 µm/s, significantly higher than SH-SAWs. Figs. 5d and 5e illustrate the reconstructed streamlines and velocity fields induced by this R-like SAW mode, showing the characteristic two-vortex flow [24] observed for both SH-SAW and R-like SAW. These patterns are clearer and more symmetrical for the R-like SAW, likely due to its more efficient coupling.

Table 2 presents the average fluid speeds (detected through the beads) relative to the SAW power for each acoustic mode. For both waves, we observed a linear relationship between streaming velocity and applied SAW power, consistent with existing literature. The values for streaming velocity and flow patterns induced by the R-like mode closely align with streaming analyses performed using pure R-SAWs on 128° Y-cut LN [25], considering similar droplet sizes and applied power. Meanwhile, SH-SAW induced streaming corroborates previous findings for shear waves in 36° Y-cut LT.

The response of the two acoustic modes to external changes, particularly temperature variations, contributes to their comprehensive characterization. SH-SAWs display a temperature coefficient of frequency (TCF) of −68.5 ± 0.4 ppm/°C, which aligns with the −70 ppm/°C reported in the Roditi datasheet for 64° Y-cut Lithium Niobate (LN) [26]. On the other hand, the Rayleigh-like SAW mode exhibits a higher TCF of −84 ± 1 ppm/°C. This value is closer to that of Rayleigh SAWs in 128° Y-cut LN, indicating potentially greater sensitivity in detecting external changes.

5. Conclusions

In conclusion, we have discovered a new configuration with IDTs oriented perpendicularly to X-axis, which can excite Rayleigh-like

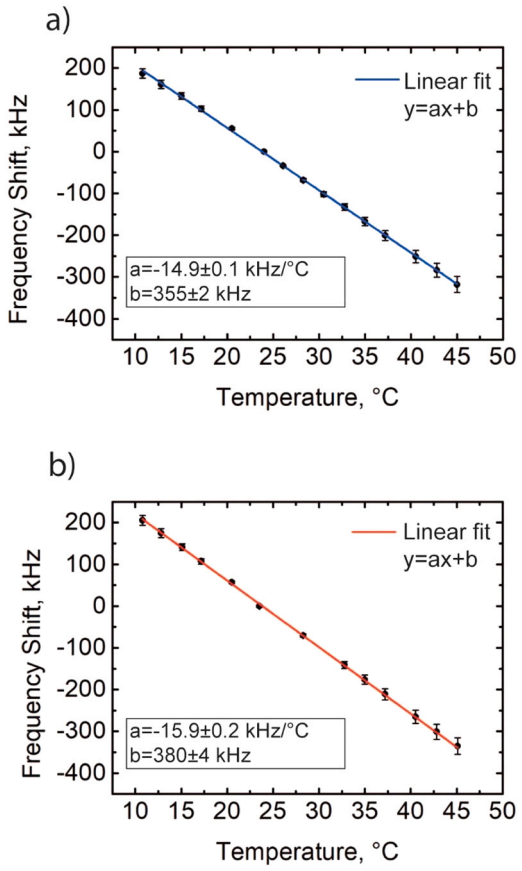

Fig. 6. The Temperature Coefficient of Frequency (TCF) for each acoustic wave, measured through changes in temperature using a temperature controller and a Peltier cell. The reported shifts in frequency are aligned with variations observed in the S11 frequency spectrum.

Table 2
Average bead velocities within the droplet, as determined by PIV analysis, in relation to the varying power levels applied to the IDTs.

Power [dBm]	Average velocity induced by SH-SAW [μm]	Average velocity induced by R-SAW [μm]
0	41±2	370±20
10	450±20	2700±100
15	660±30	11400±500

SAWs.

We started with the analysis of the principal SH-SAW mode, then with the help of finite element simulations (FEM), we investigated different IDTs orientations in order to explore other acoustic modes. We demonstrated that IDTs oriented along the y-direction can generate Rayleigh-like mode and we conducted a complete characterization of this acoustic wave. This characteristic makes the 64° Y-cut lithium niobate a promising substrate for dual-mode systems, capable of carrying out sensing, mixing, and simultaneous detection in different environments (wet and dry).

The main characteristics of the two modes are summarized in Table 3.

SH-SAWs present a principal displacement component alongside the plane parallel to the propagation direction. This property produces a weak attenuation in liquid which makes SH-SAWs suitable for sensing in wet environments. However, this wave can induce acoustic streaming (although weak) due to a displacement component normal to the surface.

The novel Rayleigh-like SAW mode presents a principal component of displacement normal to the surface, a no-leaky trend along with the propagation, and a high coupling in liquid (which produces efficient streaming). These characteristics are comparable with those of the well-known R-SAWs mode in substrates like 128° Y-cut LN.

The simulated electromecchanical coupling coefficient $\boldsymbol{k^2}$ value for the SH-SAW is consistent with what is reported in the literature (Morgan et al.), while the value for the R-like SAW is particularly interesting. Despite being a secondary mode, it exhibits a higher value compared to other substrates, such as quartz

We demonstrated that IDTs oriented perpendicular to the X-axis can generate a Rayleigh-like mode, characterized by a strong displacement normal to the surface and non-leaky propagation. This characteristic makes the 64° Y-cut lithium niobate a promising substrate for dual-mode systems capable of carrying out sensing, mixing, and simultaneous detection in different environments (wet and dry).

Building on the previously discussed works that employs both SH-SAW and R-SAW on the same piezoelectric substrates, the use of 64° Y-cut lithium niobate emerges as a significant innovation.

The advantage of employing lithium niobate lies in the substantial increase in the electromechanical coupling coefficient k^2, which determines the efficiency in generating SAW, compared to quartz and langasite. For lithium niobate cuts, the k^2 range is between 5.5 % and 17.2 % (11 % for the 64° Y-cut), whereas quartz has a k^2 value of 0.14 % and langasite has a k^2 value of 0.36 %. Although lithium tantalate has k^2 values of the same order of magnitude, the advantage of lithium niobate remains in terms of manufacturing and designing microfluidic biosensors that can generate the two acoustic waves with orthogonal transducers.

The possibility of generating dual wave modes in the same 64° Y-cut lithium niobate substrate can be exploited in high quality SAW-sensors integrated with microfluidic structures. This configuration combines sensing and mixing effects and can lead to simultaneous and multiplexing detection in different environments. Such integration enhances the efficiency and versatility of sensors, making them ideal for diverse analytical and diagnostic tasks. It can lead to more accurate and real-time analysis, improving applications in fields like biomedical diagnostics, environmental and agrifood monitoring.

CRediT authorship contribution statement

Marco Cecchini: Writing-review & editing, Supervision, Project administration, Funding acquisition, Conceptualization; **Francesco Lunardelli:** Writing – original draft, Software, Methodology, Investigation, Data curation, Conceptualization; **Matteo Agostini:**Writing – review & editing, Methodology, Investigation; **Elena Corradi:** Writing –

Table 3
Complete characterization of the two acoustic modes.

	Principal component of displacement	Damping along the propagation direction	Damping in liquid	Acoustic-streaming	TCF	k^2 From Simulations
SH-SAWs	In plane, parallel to the propagation direction	Leaky	Low attenuation in liquid	Generation of mild induced acoustic streaming	−68.5 ± 0.4 ppm/°C	9.42 ± 0.05 %
R-SAWs-like	Normal to the surface	Not leaky	High attenuation in liquid	Efficient generation of induced acoustic streaming	−84 ± 1 ppm/°C	2.15 ± 0.06 %

review & editing, Investigation.

Declaration of Competing Interest

The authors declare the following financial interests/personal relationships which may be considered as potential competing interests: Marco cecchini has patent #102023000010053 pending to Scuola Normale Superiore, CNR, INTA srl. Matteo agostini has patent #102023000010053 pending to Scuola Normale Superiore, CNR, INTA srl. Francesco Lunardelli has patent #102023000010053 pending to Scuola Normale Superiore, CNR, INTA srl. MC and MA are co-founders and own a part of INTA srl. MA is CEO and in the boards of directors of INTA srl. MC was CTO and in the boards of directors of INTA srl (04/2020–04/2023). MC is in the Scientific and Technical Committee of INTA srl. If there are other authors, they declare that they have no known competing financial interests or personal relationships that could have appeared to influence the work reported in this paper.

Data availability

Data are available at https://zenodo.org/records/11105106

Appendix A. Supporting information

Supplementary data associated with this article can be found in the online version at doi:10.1016/j.sna.2024.115780.

References

[1] David Ballantine, R. White, S. Martin, Antonio Ricco, E. Zellers, G. Frye, H. Wohljen, Acoustic Wave Sensors: Theory, Design, & Physico-Chemical Applications, Academic Press, San Diego, 1997.

[2] D. Mandal, S. Banerjee, Surface acoustic wave (SAW) sensors: physics, materials, and applications, Sensors 22 (3) (2022) 820, https://doi.org/10.3390/s22030820.

[3] X. Liu, X. Chen, Z. Yang, H. Xia, C. Zhang, X. Wei, Surface acoustic wave based microfluidic devices for biological applications, Sens. Diagn. 2 (3) (2023) 507, https://doi.org/10.1039/D2SD00203E.

[4] M. Yamaguchi, Early days of SH-type surface acoustic wave research, Jpn. J. Appl. Phys. 42 (5S) (2003) 2909, https://doi.org 10.1143/JJAP.42.2909.

[5] R.J. Shilton, M. Travagliati, F. Beltram, M. Cecchini, Nanoliter-droplet acoustic streaming via ultra high frequency surface acoustic waves, Adv. Mater. 26 (29) (2014) 4941–4946, https://doi.org/10.1002/adma.201400091.

[6] J.L. Han, H. Hu, Q.Y. Huang, Y.L. Lei, Particle separation by standing surface acoustic waves inside a sessile droplet, Sens. Actuators A: Phys. 326 (2021) 112731, https://doi.org/10.1016/j.sna.2021.112731.

[7] J.C. Hsu, Y.D. Lin, Microparticle concentration and separation inside a droplet using phononic-crystal scattered standing surface acoustic waves, Sens. Actuators A: Phys. 300 (2019), https://doi.org/10.1016/j.sna.2019.111651.

[8] T. Peng, C. Fan, M. Zhou, F. Jiang, D. Drummer, B. Jiang, Rapid enrichment of submicron particles within a spinning droplet driven by a unidirectional acoustic transducer, Anal. Chem. 93 (39) (2021) 13293–13301, https://doi.org/10.1021/acs.analchem.1c02914.

[9] David Morgan. Surface Acoustic Wave Filters, second edition, Academic Press, 2007.

[10] T. Kogai, H. Yatsuda, Liquid sensor using SAW and SH-SAW on quartz. Proceedings, IEEE Ultrason. Symp. 1 (2006) 552–555, https://doi.org/10.1109/ULTSYM.2006.143.

[11] S. Li, V.R. Bhethanabotla, Design of a portable orthogonal surface acoustic wave sensor system for simultaneous sensing and removal of nonspecifically bound proteins, Sensors 19 (18) (2019) 3876, https://doi.org/10.3390/s19183876.

[12] W. Huang, Q. Yang, J. Liao, et al., Integrated Rayleigh wave streaming-enhanced sensitivity of shear horizontal surface acoustic wave biosensors, Biosens. Bioelectron. 247 (2024) 115944, https://doi.org/10.1016/j.bios.2023.115944.

[13] T. Kogai, H. Yatsuda, J. Kondoh, Rayleigh SAW-Assisted SH-SAW Immunosensor on X-Cut 148-Y LiTaO3, IEEE Trans. Ultrason Ferroelectr. Freq. Control 64 (9) (2017) 1375–1381, https://doi.org/10.1109/TUFFC.2017.2734282.

[14] R. Singh, S.K.R.S. Sankaranarayanan, V.R. Bhethanabotla, Orthogonal surface acoustic wave device based on langasite for simultaneous biosensing and biofouling removal, Appl. Phys. Lett. 94 (26) (2009) 263503, https://doi.org/10.1063/1.3160735.

[15] K. Yamanouchi, K. Shibayama, Propagation and amplification of rayleigh waves and piezoelectric leaky surface waves In LiNbO3, J. Appl. Phys. 43 (3) (1972) 856–862, https://doi.org/10.1063/1.1661294.

[16] Z. Ramshani, A.S.G. Reddy, B.B. Narakathu, J.T. Wabeke, S.O. Obare, M. Z. Atashbar, SH-SAW sensor based microfluidic system for the detection of heavy metal compounds in liquid environments, Sens. Actuators B: Chem. 217 (2015) 72–77, https://doi.org/10.1016/j.snb.2014.12.026.

[17] Daryl L. Logan, A first course in the finite element method, PWS Engineering, Boston, 1986.

[18] T. Wang, R. Green, R.R. Nair, et al., Surface acoustic waves (SAW)-based biosensing for quantification of cell growth in 2D and 3D cultures, Sensors 15 (12) (2015) 32045–32055, https://doi.org/10.3390/s151229909.

[19] Y.Q. Fu, J.K. Luo, N.T. Nguyen, A.J. Walton, A.J. Flewitt, X.T. Zu, Y. Li, G. McHale, A. Matthews, E. Iborra, H. Du, W.I. Milne, Advances in piezoelectric thin films for acoustic biosensors, acoustofluidics and lab-on-chip applications, Prog. Mater. Sci. 89 (2017) 31–91, https://doi.org/10.1016/j.pmatsci.2017.04.006.

[20] N. Belkhelfa, R. Serhane, Process and device simulation of SAW temperature sensors compatible with 1 μm CMOS technology, Eng. Proc. 14 (1) (2022) 9, https://doi.org/10.3390/engproc2022014009.

[21] J. Koskela, V.P. Plessky, M.M. Salomaa, Suppression of the leaky SAW attenuation with heavy mechanical loading, IEEE Trans. Ultrason Ferroelectr. Freq. Control 45 (2) (1998) 439–449, https://doi.org/10.1109/58.660154.

[22] M. Agostini, M. Cecchini, Ultra-high-frequency (UHF) surface-acoustic-wave (SAW) microfluidics and biosensors, Nanotechnology 32 (21) (2021) 312001, https://doi.org/10.1088/1361-6528/abfaba.

[23] D.S. Brodie, Y.Q. Fu, Y. Li, M. Alghane, R.L. Reuben, A.J. Walton, Shear horizontal surface acoustic wave induced microfluidic flow, Appl. Phys. Lett. 99 (15) (2011) 153704, https://doi.org/10.1063/1.3651487.

[24] T. Frommelt, D. Gogel, M. Kostur, P. Talkner, P. Hanggi, A. Wixforth, Flow patterns and transport in Rayleigh surface acoustic wave streaming: combined finite element method and raytracing numerics versus experiments, IEEE Trans. Ultrason., Ferroelectr., Freq. Control 55 (10) (2008) 2298–2305, https://doi.org/10.1109/TUFFC.928.

[25] V. Mišeikis, R.J. Shilton, M. Travagliati, et al., Acoustic streaming of microparticles using graphene-based interdigital transducers, Nanotechnology 32 (37) (2021), https://doi.org/10.1088/1361-6528/ac0473.

[26] Lithium Niobate Properties, roditi. https://www.roditi.com/SingleCrystal/LiNbO3/liNBO3-Properties.html.

Francesco Lunardelli He was born in La Spezia on 07/03/1995. He earned his bachelor's degree in Physics from the University of Pisa in 2017 and completed his master's degree in Condensed Matter Physics at the same university in 2020. From September 2020 to September 2021, he worked as a research fellow at CNR, Nanoscience Institute in Pisa. Since 2021, I've started a Ph.D. program in Nanoscience at the Scuola Normale Superiore (Pisa, Italy). My thesis project is focused on developing micro and nanostructured biosensors using surface wave technology (SAW).

Matteo Agostini is the CEO and co-founder of INTA Systems, a spin-off from the National Research Council of Italy (CNR) and the Scuola Normale Superiore University of Pisa (SNS). He holds a degree in Electronic and Industrial Nanotechnology Engineering from La Sapienza University of Rome and a PhD in Molecular Biophysics from SNS. INTA Systems develops and markets innovative on-chip molecular diagnostics devices for detecting viruses, bacteria, or biomarkers in biological fluids.

Elena Corradi was born in Rome in 1993. She has studied Matter Physics at the University of Pisa and she got her Master degree in 2018. She developed her Master thesis in the UK (Harwell Campus, Oxfordshire), where she took experiments on UV solar irradiance for healthcare applications. From 2019, she is a PhD candidate in Nanoscience at Scuola Normale Superiore, Pisa (Italy), in collaboration with Fondazione Pisana per la Scienza, San Giuliano Terme (Italy). Her current research interests are biosensors, bioinformatics, and statistical models applied to high-throughput sequencing data.

Marco Cecchini Born in Italy in 1975, he earned his Master's degree in Physics from the Physics Department of the University of Pisa (Italy) in 1999, followed by a PhD in Condensed Matter Physics from the Scuola Normale Superiore (Italy) in 2006. Currently, he holds the position of senior researcher and is a member of the scientific council at the Nanoscience Institute in Pisa, Italy, which is part of the Italian National Research Council (CNR). Additionally, he is a Lecturer of Biomaterial Science within the Biology Department at the University of Pisa for the Laurea Degree Course in Molecular Biotechnology. He is a co-founder of INTA srl, a joint spin-off company of CNR and Scuola Normale Superiore, where he served on the director board and as Chief Technology Officer from 2020 to 2023, and now continues as a scientific advisor. His primary research interests lie in the development of nanomaterials for brain pathologies and nerve regeneration, as well as in the advancement of surface-acoustic-wave devices for microfluidics and sensing applications.